Progress In Electromagnetics Research B, Vol. 83, 25–42, 2019

Multi-Objective Optimization of Wireless Power Transfer Systems with Magnetically Coupled Resonators and Nonlinear Loads

Johan Winges[1, *], Thomas Rylander[1], Carl Petersson[2], Christian Ekman[2], Lars-Åke Johansson[2], and Tomas McKelvey[1]

Abstract—We present an optimization procedure for wireless power transfer (WPT) applications and test it numerically for a WPT system design with four resonant circuits that are magnetically coupled by coaxial coils in air, where the magnetic field problem is represented by a fully populated inductance matrix that includes all magnetic interactions that occur between the coils. The magnetically coupled resonators are fed by a square-wave voltage generator and loaded by a rectifier followed by a smoothing filter and a battery. We compute Pareto fronts associated with a multi-objective optimization problem that contrasts: 1) the system efficiency; and 2) the power delivered to the battery. The optimization problem is constrained in terms of: 1) the physical construction of the system and its components; 2) the root-mean-square values of the currents and voltages in the circuit; and 3) bounds on the overtones of the currents in the coils in order assure that the WPT system mainly generates magnetic fields at the operating frequency. We present optimized results for transfer distances from 0.8 to 1.6 times the largest coil radius with a maximum power transfer from 4 kW to 9 kW at 85 kHz, which is achieved at an efficiency larger than 90%.

1. INTRODUCTION

Wireless transmission of electrical energy from a source to a device has received increased attention in recent years [1]. The current interest of wireless power transfer (WPT) is mainly focused on devices with batteries that require frequent charging such as mobile phones, laptops, medical implants, vehicles and trains. For short-range applications, contactless power transfer systems [2] are relatively mature and used in many commercial applications today. Naturally, it is desirable to extend this technology to situations that feature a significantly larger distance between the source and the device, which often are referred to as mid-range applications. One promising technique for mid-range applications such as wireless charging of electric vehicles is inductive power transfer systems with magnetically coupled resonators [3, 4].

For a very challenging problem in terms of power transfer distance, Kurs *et al.* [5] transfer 60 W at an efficiency of about 40% for $d/r_{\max} = 8$, where $r_{\max}$ is the radius of the two resonant coils that they use, and d is the distance between the source coil and the device coil. Kesler [6] presents an analysis of this system in terms of circuit theory, where it is assumed that: 1) the source and the device circuits are resonant at the oscillation frequency of the generator; and 2) the generator resistance and load resistance can be chosen in a favorable manner. Given this situation, the efficiency is $\eta = U^2/(1+\sqrt{1+U^2})^2$, where $U = k_{12}\sqrt{Q_1 Q_2}$ for the coupling coefficient k_{12} and the quality factors Q_i of the source and the device. For applications that require higher power delivered to the load, it is desirable to increase the efficiency in order to avoid excessive heating of the WPT system. Should high Q_i be maintained for the

Received 15 November 2018, Accepted 11 January 2019, Scheduled 17 January 2019
* Corresponding author: Johan Winges (winges@chalmers.se).
[1] Department of Electrical Engineering, Chalmers University of Technology, SE-412 96, Göteborg, Sweden. [2] QRTECH AB, Flöjelbergsgatan 1c, SE-431 35, Mölndal, Sweden.

source and the device, high efficiency can be accomplished for systems with lower $d/r_{\max}$, since such geometrical configurations make it possible to increase k_{12} substantially. A number of options have been presented for $d/r_{\max} \simeq 1$ and, typically, these systems target the wireless charging of vehicles [3, 7]. For $d/r_{\max} = 0.5$, Bosshard *et al.* [8] demonstrate an optimized WPT system capable of transferring up to 5 kW at an efficiency of 96%.

The WPT systems [3, 5–8] exploit $N_{\mathrm{r}} = 2$ resonant circuits, where one is located on the primary side of the system (i.e., the source) and the other on the secondary side of the system (i.e., the device). Kiani and Ghovanloo [9] demonstrate a system with N_{r} resonant circuits that are magnetically coupled and, for the range $2 < d/r_{\max} < 4$, they achieve a higher efficiency for $N_{\mathrm{r}} = 3$ and 4 as compared to $N_{\mathrm{r}} = 2$, which may be attributed to the additional degrees of freedoms associated with the extra resonant circuits. However, the analysis presented by Kiani and Ghovanloo [9] requires that: 1) all the resonant circuits are resonant at the oscillating frequency of the generator; and 2) each coil only couples magnetically to its immediate neighbors, which yields a tridiagonal inductance matrix that simplifies the analysis. These prerequisites make it possible to arrive at analytic expressions for the efficiency by means of coupled mode theory [5] or reflected load theory [10]. Based on these principles, Hui *et al.* [11] demonstrate a relay arrangement for WPT with a larger number of magnetically coupled resonant circuits, where $2 \leq N_{\mathrm{r}} \leq 8$. Additional analytic derivations for multi-coil relay WPT systems can be found in [12, 13]. Frequency splitting [11, 14] has been identified as a design problem for WPT systems with multiple resonant circuits that share the same resonant frequency. If frequency splitting occurs, the power delivered to the load may become significantly reduced, unless for example the generator frequency is increased or decreased as a means of compensation. This may be problematic for applications where regulations require that the WPT is carried out at a fixed frequency.

In this article, we present a constrained multi-objective optimization procedure for nonlinear WPT systems that contrasts the two objectives: 1) the system efficiency; and 2) the power delivered to the battery. The WPT system is modeled by a set of magnetically coupled resonators fed by a square-wave voltage source (that models the power inverter) and loaded by a rectifier followed by a smoothing filter and a simple battery model, which yields a nonlinear WPT system-model. Our optimization problem is subjected to practically realistic constraints on: 1) the physical construction of the system and its components; 2) the root-mean-square values of the currents and voltages in the circuit; and 3) bounds on current overtones in the coils. The constraints are determined by the application and they are not only important from a practical perspective, but they also have a significant impact on the optimized designs. In relation to the optimization objectives, we note that Hui *et al.* [11] argue that it is important to maximize the output power for large $d/r_{\max}$ and that it is typically easier to achieve high efficiency. We find that our multi-objective optimization approach is useful since it exposes the performance limitations of the WPT system in regards to both power transfer and efficiency, where the system design is subject to the constraints for the application at hand. This is unusual in the open literature, where an exception is the work by Bosshard *et al.* [8, 15] for $N_{\mathrm{r}} = 2$.

We employ genetic algorithms [16, 17] to solve this multi-objective optimization problem for the time-periodic state that follows after the transient stage when the WPT system is energized. In the context of the optimization problem, the resonance frequencies of the magnetically coupled resonators are allowed to be independent of each other and the oscillation frequency of the generator. This is in stark contrast to many analytical results found in the literature such as [9, 18, 19], where the resonance frequencies of all resonators are forced to be equal to the generator frequency. Given a resistive load connected directly to the power inverter, we derive expressions for the optimal load resistance subject to constraints on the generator's current and voltage. Our optimization procedure retrieves this optimal load resistance approximately for the WPT systems considered in this article, and to the best of our knowledge, this type of results is not available in the open literature.

We test our optimization procedure on a family of WPT systems with $0.8 \leq d/r_{\max} \leq 1.6$, which yield a magnetic coupling coefficient across the air-gap that range approximately from 5% to 17%. This family of coil arrangements can be used for the charging of regular cars and suburban utility vehicles (SUVs), which may be deduced from the limited area available under the vehicle in combination with the distance between the vehicle and the ground. Within this context, we target wireless charging for power levels that encompass both the 3.6 kW and 7.7 kW levels at the frequency 85 kHz, as defined by the SAE standard J2954 [20]. In addition, we wish that a physical implementation of the system

can be based on rather standard off-the-shelf components in order to achieve a modest over-all cost for the WPT system, which in turn implies a number of rather severe constraints on the currents and voltages for the various components and subsystems of the WPT system. Moreover, we constrain the current overtones in the coils to ensure that the WPT system mainly generates magnetic fields in the frequency band 81–90 kHz in accordance to the SAE standard [20]. In order to simultaneously fulfill these objectives and constraints, we use $N_{\mathrm{r}} = 4$ magnetically coupled resonance circuits. To facilitate for large scale optimization, we use a simple coil model with four circular coaxial coils in free space, which can be accurately described with Biot-Savart's law [21]. Naturally, a realistic WPT system intended for wireless charging of vehicles requires magnetic materials to guide the magnetic fields in the proximity of the metal chassis of the vehicle. However, the coil system in free space yields reasonable results for the magnetic coupling coefficient as compared to geometrically similar systems that use magnetic materials, where the magnetic coupling coefficient is the most important circuit parameter derived from the field problem. Also, it should be emphasized that our optimization procedure works equally well for WPT systems that use magnetic materials that require additional computational cost associated with the more involved field problem. The coil and circuit model employed in this article have been experimentally verified in [22], where we presented a (non-optimal) four coil WPT system capable of transferring 3.4 kW at 91% system efficiency to a resistive load. The circuit model was also experimentally verified in [23], where we show that a safe magnetic field strength is possible to realize at the edge of a small vehicle for a 3 kW WPT system using magnetic materials. In this article, we present simulated results with optimal power transfer and efficiency for a range of transfer distances to a battery load.

2. SYSTEM MODEL

Figure 1 shows a schematic diagram of the WPT system that consists of: 1) a power inverter; 2) a set of magnetically coupled resonators; and 3) a rectifier with a filter connected to the load. The power inverter is fed by a constant voltage source.

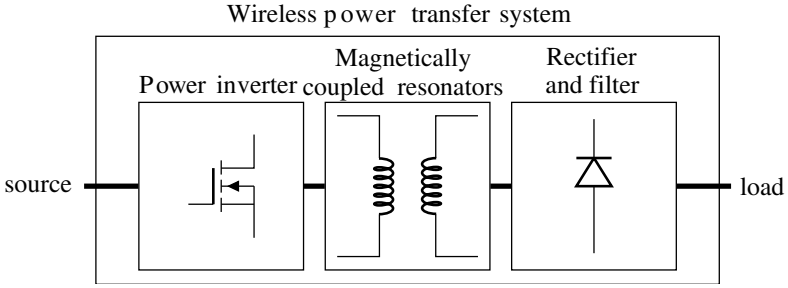

Figure 1. Schematic diagram for the wireless power transfer system.

2.1. Power Inverter

The power inverter is modeled by a voltage source $u_{\mathrm{G}}(t)$ in series with a resistance R_{G} as shown in Figure 2(a), where the square-wave voltage is given by

$$u_{\mathrm{G}}(t) = U_0 \operatorname{sgn}\left[\cos(\omega_{\mathrm{p}} t)\right]. \tag{1}$$

Here, the angular frequency is $\omega_{\mathrm{p}} = 2\pi f_{\mathrm{p}}$, and the corresponding period is $T_{\mathrm{p}} = 1/f_{\mathrm{p}}$ for a power inverter that operates at the frequency f_{p}. The power inverter is constrained by the maximum voltage amplitude $U_0^{\max}$ such that $U_0 \leq U_0^{\max}$.

2.2. Magnetically Coupled Resonators

The circuit diagram of the magnetically coupled resonators is shown in Figure 2(b). Here, we use $N = 4$ according to the motivation given in the introduction. However, the circuit diagram and its analysis described below are easy to generalize to arbitrary integer $N \geq 2$. The terminals A_1–A_2 are connected

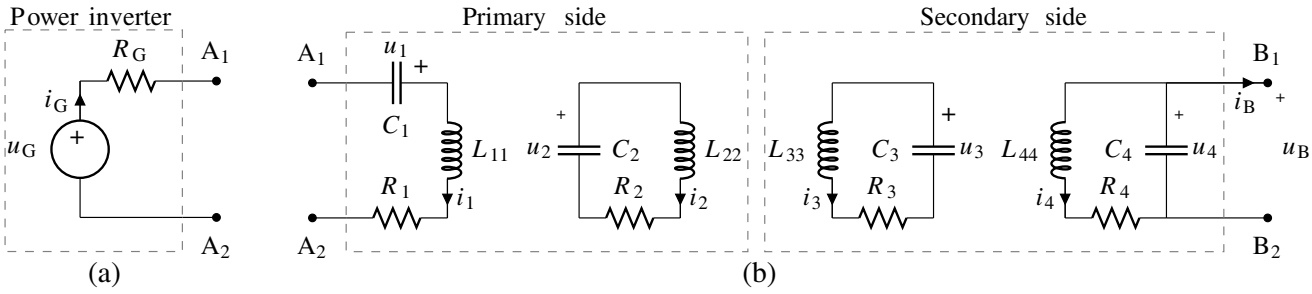

Figure 2. Circuit diagram for: (a) the power inverter; and (b) the magnetically coupled resonators.

to the power inverter and, in our case with $N = 4$, the dashed box contains the components associated with the primary side. The secondary side is indicated by the dashed box with the terminals B_1–B_2, which are connected to a load that is characterized by $i_B = i_B(u_B)$ with $u_B = u_4$. Thus, we have the circuit model

$$\mathbf{L}\frac{\partial \mathbf{i}}{\partial t} = \mathbf{u} - \mathbf{R}\mathbf{i} + \mathbf{u}_G, \tag{2}$$

$$\mathbf{C}\frac{\partial \mathbf{u}}{\partial t} = -\mathbf{i} - \mathbf{i}_B(u_B), \tag{3}$$

where the state of the circuit is described by the current vector $\mathbf{i} = [i_1, i_2, i_3, i_4]^T$ and the voltage vector $\mathbf{u} = [u_1, u_2, u_3, u_4]^T$. Further, we have the excitation voltage vector $\mathbf{u}_G = [u_G, 0, 0, 0]^T$ and the load current vector $\mathbf{i}_B(u_B) = [0, 0, 0, i_B(u_B)]^T$. The diagonal matrices $\mathbf{C} = \mathrm{diag}(C_1, C_2, C_3, C_4)$ and $\mathbf{R} = \mathrm{diag}(R_G + R_1, R_2, R_3, R_4)$ represent the capacitors and resistors, respectively. Finally, the self and mutual inductances are represented by the inductance matrix $\mathbf{L}$, which is a fully populated matrix to account for all magnetic coupling within and between the primary and secondary sides.

2.3. Load Models

The simplest load is a resistor R_L connected directly to the terminals B_1-B_2. Then, $i_B(u_B) = G_L u_B$ with the conductance $G_L = 1/R_L$ and we have $\mathbf{i}_B = \mathbf{G}\mathbf{u}$ in Eq. (3), where $\mathbf{G} = \mathrm{diag}(0, 0, 0, 1/R_L)$. Consequently, Eqs. (2)–(3) can be solved as a linear circuit for a time-harmonic excitation.

For situations that involve charging of a battery, we consider a full-wave rectifying circuit that consists of four diodes with a smoothing filter connected to a simple model of a battery as shown in Figure 3. The battery is modeled by an internal resistance R_B and an electromotive force $\mathcal{E}_B$. For the diodes shown in Figure 3, we use a piecewise linear current-voltage characteristic

$$i_D = i_D(u_D) = \begin{cases} 0 & \text{if } u_D \le u_{FB}, \\ (u_D - u_{FB})/R_D & \text{if } u_D > u_{FB}, \end{cases} \tag{4}$$

where u_{FB} is the forward-bias voltage-drop and R_D is the forward resistance.

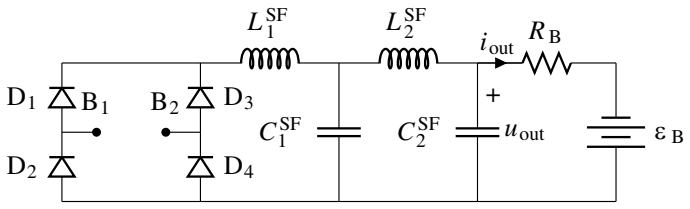

Figure 3. Load circuit with full-wave rectifier followed by a smoothing filter and a simple model of a battery.

3. METHOD

3.1. Time-Domain Analysis and Modelling

The circuit model in Eqs. (2)–(3) together with the generator and load model yields a time-domain representation of the system that can be expressed as a state-space model, where the currents through inductors and the voltages over capacitors are collected in a single state vector $\mathbf{y}(t)$. The state-space model can be written as a system of coupled ordinary differential equations on the form

$$\dot{\mathbf{y}}(t) = \mathbf{A}(\mathbf{y}(t))\mathbf{y}(t) + \mathbf{B}(\mathbf{y}(t))\mathbf{x}(t), \tag{5}$$

where the matrices $\mathbf{A}$ and $\mathbf{B}$ depend on the state vector $\mathbf{y}(t)$, i.e., if the diodes in the circuit are conducting or not. Sources are collected in the forcing vector $\mathbf{x}(t)$.

For a time interval of unchanged conduction states for the diodes, we have a linear circuit (given our piecewise linear model for the diodes) and the matrices $\mathbf{A}$ and $\mathbf{B}$ are constant. Then, the solution of Eq. (5) for $t \geq t_i$ is

$$\mathbf{y}(t) = \mathbf{F}(t)\mathbf{y}(t_i) + \int_{t_i}^{t} \mathbf{F}(t-\tau)\mathbf{B}\mathbf{x}(\tau)d\tau, \tag{6}$$

where $\mathbf{y}(t_i)$ is the initial state, and we have introduced the matrix exponential $\mathbf{F}(t) = e^{\mathbf{A}(t-t_i)}$. We construct an explicit time-stepping scheme based on the state-space model of Eq. (5) and its explicit solution of Eq. (6), where we assume that $\mathbf{x}(t)$ is constant for $t \geq t_i$. Given a finite time-step Δt, we update the solution according to Eq. (6) from t_i to $t_{i+1} = t_i + \Delta t$. As a default value, we use $\Delta t = T_\mathrm{p}/N$ with $N = 512$, and if needed for convergence, we increase N by a factor 2^k for a positive integer k and restart the simulation. At every time step, the conduction conditions for the diodes are evaluated, and $\mathbf{A}, \mathbf{B}$ and $\mathbf{x}$ are changed accordingly. The time stepping is stopped after the transients have vanished, and the voltages and currents are time-periodic with a relative tolerance of 10^{-3}.

For the time-periodic currents and voltages, we are interested in the input and output power and the system efficiency

$$\bar{p}_\mathrm{in} = \langle\, p_\mathrm{in}(t)\,\rangle = \frac{1}{T_\mathrm{p}} \int_{t_0}^{t_0+T_\mathrm{p}} u_\mathrm{in}(t) i_\mathrm{in}(t) dt, \tag{7}$$

$$\bar{p}_\mathrm{out} = \langle\, p_\mathrm{out}(t)\,\rangle = \frac{1}{T_\mathrm{p}} \int_{t_0}^{t_0+T_\mathrm{p}} u_\mathrm{out}(t) i_\mathrm{out}(t) dt, \tag{8}$$

$$\eta = \frac{\langle\, p_\mathrm{out}(t)\,\rangle}{\langle\, p_\mathrm{in}(t)\,\rangle}, \tag{9}$$

where $\langle\,\cdot\,\rangle$ denotes the time average for one period from t_0 to $t_0 + T_\mathrm{p}$, and it is assumed that the system is time-periodic for $t \geq t_0$. Here, $u_\mathrm{in}(t) = u_\mathrm{G}(t)$ and $i_\mathrm{in}(t) = i_\mathrm{G}(t)$, where u_G and i_G are defined in Figure 2(a). The output voltage and current are defined in Figure 3.

3.1.1. Time-Harmonic Representation

A signal $s(t)$ (i.e., a current or voltage) that is time-periodic can be decomposed in a Fourier series $\sum_n c_n \exp[j2\pi nt/T_\mathrm{p}]$. For the fundamental mode of $s(t)$, we use phasor notation and introduce the complex amplitude $\hat{s} = 2c_1$, which corresponds to the part of the signal that is useful for the power transfer. In addition, we denote the effective value of the phasor by $\tilde{s} = \hat{s}/\sqrt{2}$. In order to assure that the WPT system mainly produces magnetic fields at the operational frequency, we find it useful to extract the undesired overtones as

$$\delta s(t) = s(t) - \mathrm{Re}\left\{ \hat{s} \exp\left[j\frac{2\pi t}{T_\mathrm{p}} \right] \right\}, \tag{10}$$

in order to impose constraints on $\delta s(t)$ when necessary.

In addition, we wish to characterize a nonlinear load given that the transients have vanished and that we have reached a time-periodic state. Thus, we find it useful to consider the impedance $Z = \hat{u}/\hat{\imath}$ given the phasors at the terminals of the load.

We note that in practice, the equivalent load impedance Z_A connected to the terminals A_1-A_2 of the power inverter is required to have $\angle Z_\mathrm{A} \geq 0^\circ$ to achieve inductive operation of the power inverter and zero-voltage-switching [15, 24].

3.2. Optimization

We optimize the WPT system in terms of the two objectives given by Eqs. (8) and (9) that depend on the time-periodic circuit state $\mathbf{y}(t)$. It should be noted that these two objectives are conflicting [11] in the sense that their extrema do not, in general, coincide. The objective functions can be organized in a vector $\mathbf{g} = [g_1, g_2]$ according to $g_1(\mathbf{p}) = \bar{p}_\mathrm{out}(\mathbf{p}; \mathbf{q})$ and $g_2(\mathbf{p}) = \eta(\mathbf{p}; \mathbf{q})$. Here, $\mathbf{p}$ describes the design of the system in terms of component values and other design parameters that are subject to optimization, and $\mathbf{q}$ describes design parameters that are not subject to optimization such as: 1) different load conditions, and 2) varying power transfer distance d.

Both the objective functions in $\mathbf{g}(\mathbf{p})$ are constructed to be used in the context of a maximization problem, and we have the multi-objective optimization problem

$$\begin{aligned} &\max_{\mathbf{p}} \ [g_1(\mathbf{p}), g_2(\mathbf{p})] \\ &\text{s.t. } \mathbf{y}(t) = \text{time-periodic circuit solution described by } \mathbf{p}, \\ &\quad \mathbf{p}_\mathrm{L} \leq \mathbf{p} \leq \mathbf{p}_\mathrm{U}, \\ &\quad U_0 = U_0^*(\mathbf{p}), \end{aligned} \tag{11}$$

which involves explicit constraints $(\mathbf{p}_\mathrm{L}, \mathbf{p}_\mathrm{U})$ on the component values directly or their geometrical design parameters. Given a specific system design described by $\mathbf{p}$, the maximum amplitude $U_0^*(\mathbf{p})$ that can be used by the power inverter is determined by an inner optimization problem

$$\begin{aligned} U_0^* = &\max_{U_0} \ U_0 \\ &\text{s.t. } \mathbf{y}(t) = \text{time-periodic circuit solution described by } \mathbf{p}, \\ &\quad \mathbf{c}(\mathbf{y}(t)) \leq \mathbf{c}_\mathrm{U}, \\ &\quad U_0 \leq U_0^\mathrm{max}. \end{aligned} \tag{12}$$

Here, the constraints $\mathbf{c}$ on the state vector $\mathbf{y}(t)$ are expressed in terms of the root-mean-square (rms) value of currents and voltages in the circuit, which clearly depend on U_0. The rms value is defined as $\langle \cdot \rangle_\mathrm{rms} = \sqrt{\langle (\cdot)^2 \rangle}$.

We solve the optimization problem in Eq. (11) by a genetic algorithm (GA) [17, 25] and the inner optimization problem in Eq. (12) that features the nonlinear constraints by bisection [26]. Given the resonant nature of the WPT system, the optimization problem features many local extrema, and thus, it is useful to exploit GAs. In addition, GAs can handle optimization problems with mixed integer and real-valued parameters, which is required for the WPT system that we consider in this article.

In this article, we do not include the constraint $\angle Z_\mathrm{A} \geq 0^\circ$ that is required to ensure inductive operation of the power inverter. This choice is based on the following experiences: 1) the optimal solutions typically yield $\angle Z_\mathrm{A} \simeq 0^\circ$; 2) enforcing this constraint severely reduces the convergence speed of the genetic optimization algorithm employed; and 3) A small negative angle $\angle Z_\mathrm{A} > -10^\circ$ can typically be compensated for without significant loss of performance by increasing the C_1 capacitance value. In an effort to assure that inductive operation is realizable, any solutions with $\angle Z_\mathrm{A} \leq -10^\circ$ have been removed after optimization.

4. RESULTS

Below, we present results for two cases: 1) a linear circuit with time-harmonic excitation and an approximately equivalent load resistance R_L; and 2) a nonlinear circuit with the time-periodic excitation in Eq. (1) and the battery load shown in Figure 3. Further, we demonstrate a simple C_1 compensation scheme that can be used to achieve inductive operation of the power inverter and present some details with respect to charging a battery with varying voltage. The results are presented for a particular test problem, which is described and motivated first.

4.1. Test Problem

In the following subsections we present the choice of component models and constraints that describe the test problem considered in this article, where our choices are motivated by wireless charging systems for electric vehicles. We stress that the coil and circuit model employed in this article have been experimentally verified in [22], where we presented a non-optimal four coil WPT system capable of transferring 3.4 kW at 91% system efficiency to a resistive load at the transfer distance $d/r_{\max} = 0.4$. Here, we consider the optimization of a similar WPT system design where larger transfer distances and power levels are feasible.

4.1.1. Power Inverter

The power inverter operates at the frequency $f_{\rm p} = 85\,\text{kHz}$ with a maximum voltage amplitude of $U_0^{\max} = 450\,\text{V}$. Thus, we have the phasor $\hat{u}_{\rm G}^{\max} = (4/\pi)U_0^{\max}$ for the fundamental mode and its effective value is $\tilde{u}_{\rm G}^{\max} = (2\sqrt{2}/\pi)U_0^{\max} = 405\,\text{V}$. In addition, we constrain the current for the power inverter by $\langle\, i_{\rm G}(t)\,\rangle_{\rm rms} \leq I_0^{\max} = 30\,\text{A}$. The generator resistance $R_{\rm G}$ is $0.25\,\Omega$.

Here, our choice of frequency is motivated by the SAE standard J2954 [20], which is intended to establish a common frequency band for wireless charging of light-duty vehicles. The choice of maximum voltage, current and generator resistance are motivated by a conservative design of a power inverter based on four transistors of type 45N65M5 from STMicroelectronics.

4.1.2. Magnetically Coupled Resonators

We consider an axisymmetric system of four coils in free space such that each coil consists of a single layer of windings that can be described by: 1) coordinate z_m along the axis of symmetry; 2) outer coil-radius r_m; and 3) number of turns N_m. The geometry is shown in Figure 4, where $\Delta z_{mn} = z_m - z_n$. The primary and secondary sides are separated by an air gap of distance Δz_{32}, which is subject to the constraint $\Delta z_{32} \geq d$. Thus, we can compute all the entries L_{mn} of the inductance matrix based on Biot-Savart's law [21], where the self and mutual inductances may be expressed in terms of elliptical integrals [27] as we approximate each turn in a coil by a closed circular loop. Further, Δz_{21} and Δz_{43} are required to be larger than 17 mm to assure that there is axial space between the different coils for a fixture. These geometrical design criteria allow for a relatively simple coil construction, where the coil wire can be wound around a thin cable reel similarly as shown in [22].

In an attempt to illustrate the relation between these coils in free space and the corresponding coils of an actual WPT system for the charging of electric vehicles, we consider the coils as viewed from the circuit based on their inductance matrix representation. The magnetic coupling coefficients of the coil

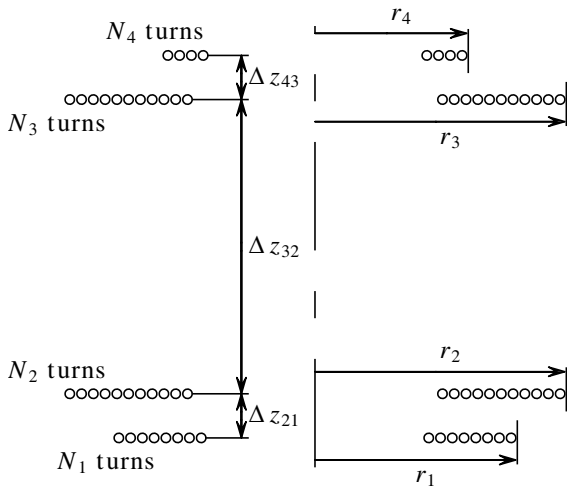

Figure 4. Geometry of the four magnetically coupled coils.

system do not change significantly as magnetic-material plates are placed, in close vicinity, below coil 1 and above coil 4. (Obviously, the magnetic materials significantly change the magnetic fields that surround the charging region between the coils.) The absolute inductances of a system with magnetic materials may be reduced (and the free space values recovered) if an appropriate number of turns are removed from each coil. Thus, a coil arrangement with magnetic materials can be constructed in such a manner that it yields an inductance matrix $\mathbf{L}_\mu$ that approximates the corresponding inductance matrix $\mathbf{L}$ of the coils in free space shown in Figure 4. For remaining deviations between the inductance matrices, possible performance reductions may be compensated for by changing the capacitances as demonstrated in [22]. Thus, an optimized WPT system based on coils in free space may be modified and implemented with magnetic materials and, thus, adopted for charging of electric vehicles. However, such a system has additional losses that stem from the magnetic materials and eddy current losses.

In a broader sense, the coils in free space provide fast analysis combined with an inductance matrix that incorporate the most important dependencies on the geometrical parameters that describe the coils. Given an optimized design presented in this article, the inductance matrix (viewed from the circuit) may be realized in terms of the electric-vehicle application that requires coils with magnetic materials, which in itself can be considered as yet another a design problem. If the performance of such a two-step procedure is not satisfying, its final design can be used as a starting point for a more refined optimization procedure that is based on a detailed field model of the WPT system together with the electric vehicle, where both magnetic and conducting materials are incorporated.

Given that Litz wire is used for the coils, the resistance of the m-th coil can be approximated as $R_m = l_m/(\sigma A)$, where σ is the bulk conductivity of the Litz-wire conductor, A the cross section of the wire, and l_m the wire length of the m-th coil. Based on the Litz-wire used in [22, 23], the diameter of the copper conductor in the Litz-wire is 4.9 mm, and we set the distance between turns in the radial direction to 5 mm. The specified Litz-wire diameter allows for a current of 60 A without excessive heating. Also, a resistance $R_0 = 0.1\,\Omega$ is added to the coil wire resistance. Here, R_0 represents an estimate of additional losses for the resonant circuits found from measurements in [22], where examples of such loss contributions are contact resistances in the circuit and the dielectric losses in the capacitors.

It is assumed that it is possible to realize the capacitances C_m for a range of values such that the frequency $f_m = 1/(2\pi\sqrt{L_{mm}C_m})$ for resonant circuit $m = 1, \ldots, 4$ can be selected between 50 kHz to 200 kHz. Here, f_m can be interpreted as the resonance frequency of the m-th resonator if *the magnetic coupling to all the other resonators is discarded*. In the context of optimization, we find it attractive to work with $f_m = 1/(2\pi\sqrt{L_{mm}C_m})$, which replaces the capacitance C_m as a design parameter given a known value for L_{mm}. Consequently, *this is nothing but a change of variables* for the optimization procedure, and it is further discussed in Section 4.1.5. Obviously, the system of magnetically coupled resonators has resonant frequencies that differ from our design parameters f_m used during optimization.

In practice, the capacitances C_m could be implemented by means of constructing a capacitor bank with, e.g., polypropylene film capacitors organized in a Cartesian grid with N_p parallel columns of N_s identical discrete capacitors connected in series. Here, N_s determines the voltage constraint and N_p the current constraint for the capacitor bank, in combination with the choice of discrete capacitors. For ease of construction, we also limit the total number of capacitors by including a constraint on the voltage-current product for each capacitor bank.

4.1.3. Rectifier, Smoothing Filter and Battery

The diodes in the rectifier are characterized in terms of the forward-bias voltage-drop $u_\mathrm{FB} = 0.92\,\mathrm{V}$ and the forward resistance $R_\mathrm{D} = 0.11\,\Omega$, where these values are motivated by the diode C4D05120A from Cree. The smoothing filter components are given by $L_1^\mathrm{SF} = 30\,\mu\mathrm{H}$, $C_1^\mathrm{SF} = 20\,\mu\mathrm{F}$, $L_2^\mathrm{SF} = 2.2\,\mu\mathrm{H}$ and $C_2^\mathrm{SF} = 10\,\mu\mathrm{F}$. The battery is modelled by an internal resistance $R_\mathrm{B} = 0.25\,\Omega$ and an electromotive force $\mathcal{E}_\mathrm{B}$ in the range of from 310 V to 390 V, which approximately represent a multi-cell lithium-ion battery for vehicles for a range of different state-of-charge (SOC).

4.1.4. Circuit Model Validation

We have compared the numeric results of the time-periodic model described in Subsection 3.1 with conventional circuit computations performed by `LTspice IV` [28] for the test problem, where `LTspice IV`

uses considerably more elaborate models for the transistors in the power inverter and the diodes in the rectifier. We find that we have less than 2% deviation between the currents and voltages in our model and the more elaborate `LTspice IV` model for the time-periodic state. The time-periodic model have also been experimentally verified for the WPT systems presented in [22, 23], where the deviations are typically less than 10% between simulation and experiment.

4.1.5. Optimization Parameters

Table 1 shows all the parameters subject to optimization and, therefore, incorporated in the parameter vector $\mathbf{p}$. It should be noted that the component values L_{mn} and R_m are computed from the coils' geometry, where the number of turns N_m is only allowed to take integer values. Further, we introduce the resonance frequency $\omega_m = 1/\sqrt{C_m L_{mm}}$ associated with the m-th resonator. We optimize with respect to $f_m = \omega_m/(2\pi)$, and then, the corresponding capacitance is determined as $C_m = 1/(\omega_m^2 L_{mm})$. This choice is based on our experience that the optimization algorithm converges in fewer iterations if we use f_m instead of C_m. The constraints for $\mathbf{p}_\mathrm{L}$ and $\mathbf{p}_\mathrm{U}$ are also listed in Table 1.

Table 1. Parameters subject to optimization in the multi-objective optimization problem (11) with minimum and maximum bounds given an application specific design box.

Component	Quantity	unit	min	max
Coil	r_m	m	0.1	0.25
	N_m	-	1	15
	Δz_{21}	m	0.017	0.1
	Δz_{32}	m	d	$d + 0.1$
	Δz_{43}	m	0.017	0.1
Resonance frequency	f_m	kHz	50	200

4.1.6. Constraints

Given this test problem, the constraints are listed in Table 2. These constraints are motivated by component limitations imposed by practical considerations and to avoid excessive heating and voltage breakdown. The constraint on the overtones $\langle\, \delta i(t) \,\rangle_\mathrm{rms}$ can be used to ensure that the WPT system mainly generates magnetic fields in the frequency band 81–90 kHz in accordance to the SAE standard [20].

Table 2. Constraints on currents and voltages for the components listed within the parentheses that are deemed appropriate for the intended power level in the WPT application.

Component	Quantity	unit	max
Coil (L_{mm}, R_m)	$\langle\, i(t) \,\rangle_\mathrm{rms}$	A	60
	$\langle\, \delta i(t) \,\rangle_\mathrm{rms}$	A	2
Capacitor (C_m)	$\langle\, u(t) \,\rangle_\mathrm{rms}$	kV	5
	$\langle\, i(t) \,\rangle_\mathrm{rms}$	A	40
	$\langle\, u(t) \,\rangle_\mathrm{rms} \langle\, i(t) \,\rangle_\mathrm{rms}$	kVA	50
Power inverter (R_G)	$\langle\, i(t) \,\rangle_\mathrm{rms}$	A	30
Rectifier (D_m)	$\langle\, u(t) \,\rangle_\mathrm{rms}$	V	850
	$\langle\, i(t) \,\rangle_\mathrm{rms}$	A	15

4.2. Linear Circuit with Time-Harmonic Excitation

According to the analysis in [8, 29], the nonlinear load in Figure 3 may be approximated as an equivalent load resistance $R_{\mathrm{L}} = (\pi \mathcal{E}_{\mathrm{B}})^2/(8\,\bar{p}_{\mathrm{out}})$. This makes it possible to construct a linear circuit that approximates the WPT system at its fundamental time-harmonic component of frequency f_{p}, and the results may be compared with the corresponding nonlinear system. Thus, we consider the four magnetically coupled resonators (shown in Figure 2(b)) fed by a time-harmonic voltage at the frequency $\omega = \omega_{\mathrm{p}}$ and loaded by a resistance R_{L} connected to the terminals B_1-B_2, which gives a linear circuit with time-harmonic excitation that we can treat in the frequency domain. The magnetically coupled resonators are subject to optimization, where we consider the range of air gap distances d between the primary and secondary sides given by $20\,\mathrm{cm} \leq d \leq 40\,\mathrm{cm}$.

Figure 5 shows Pareto fronts that contrast system efficiency η and power $\bar{p}_{\mathrm{out}}$ delivered to the resistance $R_{\mathrm{L}} = 35\ \Omega$ for relative distances in the interval $0.8 \leq d/r_{\max} \leq 1.6$. We note that η decreases monotonically as $\bar{p}_{\mathrm{out}}$ is increased, which confirms that the two objectives are conflicting. For sufficiently low values of $\bar{p}_{\mathrm{out}}$, none of the constraints in Table 2 are active. As $\bar{p}_{\mathrm{out}}$ is increased, one or several constraints become active, and the system efficiency deteriorates at a higher pace. In Figure 5, it is primarily the constraints $\langle\, u(t)\,\rangle_{\mathrm{rms}} \langle\, i(t)\,\rangle_{\mathrm{rms}}$ for $m = 1, 2, 3$ that become active. For each of the fixed value of $d/r_{\max}$, we achieve a similar Pareto front as the optimization problem is solved for a different load resistance R_{L}, where we have tested the range $15\,\Omega \leq R_{\mathrm{L}} \leq 55\,\Omega$.

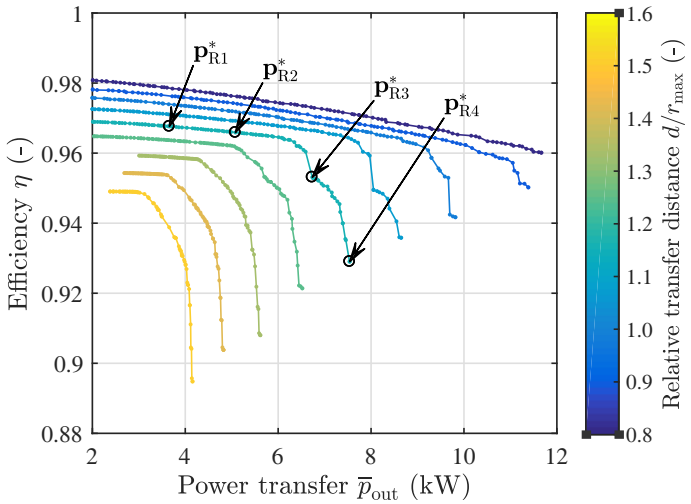

Figure 5. Pareto fronts that contrast efficiency and power delivered to the load resistance $R_{\mathrm{L}} = 35\,\Omega$ for $0.8 \leq d/r_{\max} \leq 1.6$, where $r_{\max} = 25\,\mathrm{cm}$. The magnetically coupled resonators are fed by a time-harmonic voltage and optimized subject to the constraints in Table 2.

Table 3 shows the optimized results $\mathbf{p}$ and derived circuit quantities for four designs located on the Pareto front shown in Figure 5 with $d/r_{\max} = 1.2$. For the optimized designs shown in Table 3, we note that: 1) $f_m \neq f_{\mathrm{p}}$ for all resonant circuit in contrast to the work by Kiani and Ghovanloo [9] that require $f_m = f_{\mathrm{p}}$ for all m; 2) f_1 and f_4 are reduced as the Pareto front is traversed from $\mathbf{p}^*_{\mathrm{R1}}$ to $\mathbf{p}^*_{\mathrm{R4}}$; and 3) N_1 and N_4 are both reduced slightly. In addition, $r_m = r_{\max}$ for all four coils and $N_m = N_{\max}$ for $m = 2$ and 3. We stress that the Pareto front exposes the important trade-off between power transfer and efficiency and that an appropriate Pareto-optimal solution should be selected depending on the application specifications. For example, design $\mathbf{p}^*_{\mathrm{R1}}$ (3.6 kW power transfer at 97% efficiency) could be appropriate for an efficient charging station suitable for overnight use while design $\mathbf{p}^*_{\mathrm{R4}}$ could be used for a faster charging solution with the considerably higher maximum power transfer of 7.5 kW at 93% efficiency. Naturally, if even higher power levels are to be realized, the voltage and current constraints must be increased correspondingly or a shorter transfer distance selected.

Next, we calculate an equivalent load impedance Z_{A} connected to the terminals A_1-A_2 in

Table 3. Design parameters $\mathbf{p}$ and derived circuit quantities for four optima on the Pareto front in Figure 5 for $d/r_{\max} = 1.2$.

Param.	Optimum $\mathbf{p}^*_{\mathrm{R1}}$ $\bar{p}_{\mathrm{out}} = 3.66\,\mathrm{kW}, \eta = 0.97$				Optimum $\mathbf{p}^*_{\mathrm{R2}}$ $\bar{p}_{\mathrm{out}} = 5.08\,\mathrm{kW}, \eta = 0.97$				Optimum $\mathbf{p}^*_{\mathrm{R3}}$ $\bar{p}_{\mathrm{out}} = 6.73\,\mathrm{kW}, \eta = 0.95$				Optimum $\mathbf{p}^*_{\mathrm{R4}}$ $\bar{p}_{\mathrm{out}} = 7.54\,\mathrm{kW}, \eta = 0.93$			
m	1	2	3	4	1	2	3	4	1	2	3	4	1	2	3	4
N_m	15	15	15	4	15	15	15	4	14	15	15	3	10	15	15	3
r_m [cm]	25	25	25	25	25	25	25	25	25	25	24.9	25	25	25	25	25
z_m [cm]	0	1.76	31.8	35.3	0	1.77	31.8	35.2	0	2.34	32.4	34.3	0	3.53	33.5	35.8
f_m [kHz]	131	103	87.8	195	122	107	87.9	191	113	110	94.8	137	96.7	111	95.9	126
L_{mm} [μH]	157	157	157	19	157	157	157	19	142	157	157	11.5	86.3	157	157	11.5
C_m [nF]	9.44	15.3	20.9	35.3	10.9	14.1	20.9	36.5	14	13.3	18	118	31.4	13.1	17.5	139
R_m [mΩ]	118	118	118	106	118	118	118	106	117	118	118	104	113	118	118	104
k_{1m} [%]	-	80.1	8.0	6.0	-	80.0	7.9	6.0	-	74.3	7.6	6.1	-	62.0	7.0	5.6
k_{2m} [%]	-	-	8.8	6.5	-	-	8.8	6.6	-	-	8.8	7.0	-	-	8.8	6.8
k_{3m} [%]	-	-	-	53.7	-	-	-	54.1	-	-	-	60.6	-	-	-	58.5

Figure 2(a), where Z_{A} corresponds to the magnetically coupled resonators and the load R_{L}. Figure 6 shows $Z_{\mathrm{A}} = R_{\mathrm{A}} + jX_{\mathrm{A}}$ as the Pareto front is traversed for $d/r_{\max} = 1.2$ and $d/r_{\max} = 0.8$. The curves are discontinued at the point where a higher power transfer cannot be achieved without violating the constraints. We consider the reactance to be close to zero, i.e., $X_{\mathrm{A}} \simeq 0$, for most parts of the Pareto front. Thus, we find that the generator is effectively loaded with a resistance R_{A}. Given this situation, a simple model consists of the power inverter shown in Figure 2(a) connected directly to a resistive load R_{A}. Then, the power delivered to the load is $\bar{p}_{\mathrm{out}} = \tilde{u}_{\mathrm{G}}^2 R_{\mathrm{A}}/(R_{\mathrm{G}} + R_{\mathrm{A}})^2 \simeq \tilde{u}_{\mathrm{G}}^2/R_{\mathrm{A}}$, which is shown as $Z_{\mathrm{A}} = R_{\mathrm{A}} = \tilde{u}_{\mathrm{G}}^2/\bar{p}_{\mathrm{out}}$ by the dash-dotted curve in Figure 6. Furthermore, Appendix A presents an analysis of this circuit with constraints on the generator voltage and current such that $\tilde{u}_{\mathrm{G}} \le \tilde{u}_{\mathrm{G}}^{\max}$ and $\tilde{\imath}_{\mathrm{G}} \le \tilde{\imath}_{\mathrm{G}}^{\max}$, where $\tilde{u}_{\mathrm{G}}^{\max} = 405\,\mathrm{V}$ and $\tilde{\imath}_{\mathrm{G}}^{\max} = 30\,\mathrm{A}$ for the power inverter considered here. For maximum power transfer to R_{A} in this simple circuit, we arrive at an optimal load resistance

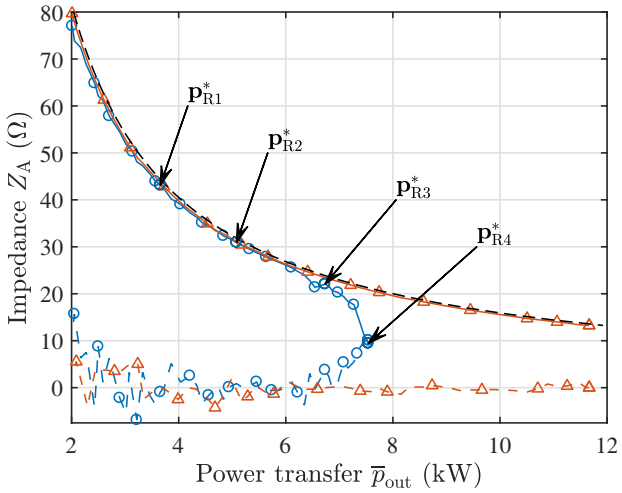

Figure 6. Impedance Z_{A} as a function of power delivered to the load resistance as the Pareto front in Figure 5 is traversed for: (○) $d/r_{\max} = 1.2$; and (△) $d/r_{\max} = 0.8$. The input impedance is computed at the terminals A_1-A_2 in Figure 2(b). The real part of the impedance is described by the solid curve and the imaginary part by the dashed curve. The black dash-dotted curve shows the load impedance $Z_{\mathrm{A}} = R_{\mathrm{A}} = \tilde{u}_{\mathrm{G}}^2/\bar{p}_{\mathrm{out}}$ for a simple generator and load model.

$R_{\mathrm{A}}^{*} = \tilde{u}_{\mathrm{G}}^{\max}/\tilde{i}_{\mathrm{G}}^{\max} - R_{\mathrm{G}} = 13.25\ \Omega$, since $\tilde{u}_{\mathrm{G}}^{\max}/\tilde{i}_{\mathrm{G}}^{\max} \geq 2R_{\mathrm{G}}$. For $d/r_{\max} = 0.8$, it is interesting to note that R_{A} approaches R_{A}^{*} for large values of $\bar{p}_{\mathrm{out}}$, which indicate that the power inverter can be optimally loaded and that primarily the generator constraints limit the maximum power transfer.

4.3. Nonlinear Circuit with Time-Periodic Excitation

Next, we consider the four magnetically coupled resonators (shown in Figure 2(b)) fed by a square-wave voltage and loaded by a rectifier followed by a smoothing filter and a battery (shown in Figure 3). The magnetically coupled resonators are subject to optimization, where we consider the range of air gap distances d between the primary and secondary sides given by $20\,\mathrm{cm} \leq d \leq 40\,\mathrm{cm}$.

Figure 7 shows Pareto fronts that contrast η and $\bar{p}_{\mathrm{out}}$ for the magnetically coupled resonators for $0.8 \leq d/r_{\max} \leq 1.6$ and $\mathcal{E}_{\mathrm{B}} = 380\,\mathrm{V}$. For each of the fixed value of $d/r_{\max}$, we achieve a similar Pareto front as the optimization problem is solved for a different electromotive force $\mathcal{E}_{\mathrm{B}}$, where we have tested the range $310\,\mathrm{V} \leq \mathcal{E}_{\mathrm{B}} \leq 390\,\mathrm{V}$. For most of the Pareto fronts, it is noted that the constraint $\langle\, \delta i(t) \,\rangle_{\mathrm{rms}}$ is active for the currents through L_{11} and L_{44}, which is reasonable since the current through L_{11} is driven by the power inverter that is rich in overtones, and L_{44} is close to the rectifier that may excite strong overtones. Also, we note that similarly as for the linear circuit, the constraints $\langle\, u(t) \,\rangle_{\mathrm{rms}} \langle\, i(t) \,\rangle_{\mathrm{rms}}$ for $m = 1, 2, 3$ become active as $\bar{p}_{\mathrm{out}}$ is increased, and thus, they limit the power transfer.

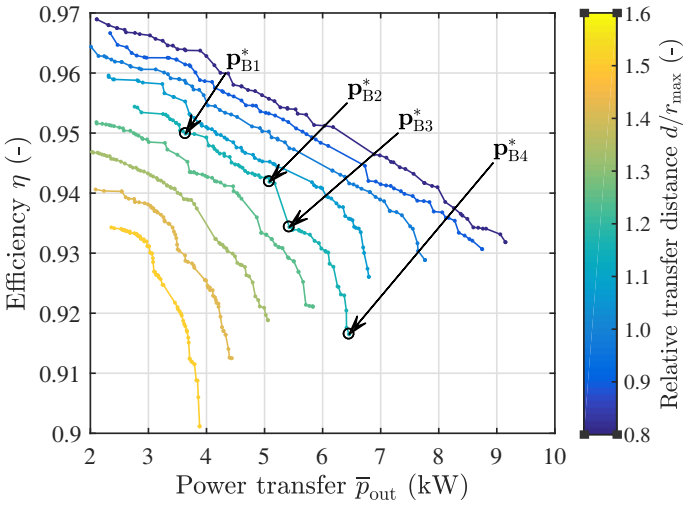

Figure 7. Pareto fronts that contrast efficiency and power delivered to the battery $\mathcal{E}_{\mathrm{B}} = 380\,\mathrm{V}$ for $0.8 \leq d/r_{\max} \leq 1.6$, where $r_{\max} = 25\,\mathrm{cm}$. The magnetically coupled resonators are fed by a square-wave voltage and optimized subject to the constraints in Table 2.

Table 4 shows the design parameters $\mathbf{p}$ and derived circuit quantities for four Pareto-optimal designs, which are indicated in Figure 7 for $d/r_{\max} = 1.2$. Interestingly, r_4 is clearly smaller than $r_{\max}$ for the nonlinear circuit, which was not the case for the linear circuit. Also, the distance Δz_{43} is about 5 cm, which is more than twice the distance found for the linear circuit. These choices combined yield a rather low coupling coefficient $0.39 \leq k_{34} \leq 0.47$ between the resonant circuit $m = 3$ and 4 for the nonlinear circuit. Furthermore, Figure 8(a) shows L_{mm} as the Pareto front ($d/r_{\max} = 1.2$) is traversed. Here, we notice in particular that L_{44} is rather small in comparison to the other inductances. Similarly, Figure 8(b) shows $\omega_m/\omega_{\mathrm{p}}$. Typically, we notice rather gradual changes in ω_m as the Pareto front is traversed and that $\omega_m > \omega_{\mathrm{p}}$ for all resonators m. It is interesting to note that the values for L_{mm} are rather similar to the time-harmonic case, which nevertheless features a somewhat similar load at ω_{p}. However, the values for $\omega_4/\omega_{\mathrm{p}}$ are significantly smaller and, as a consequence, C_4 is now larger for the nonlinear circuit. One possible interpretation of this result is that a larger C_4 yields a rather low impedance in parallel with the inductance L_{44}, which in turn makes the capacitor C_4 act as a sink for current overtones produced by the rectifier that otherwise would flow through the inductance L_{44}. We

Table 4. Design parameters $\mathbf{p}$ and derived circuit quantities for four optima on the Pareto front in Figure 7 for $d/r_{\max} = 1.2$.

Param.	Optimum $\mathbf{p}^*_{\mathrm{B1}}$ $\bar{p}_{\mathrm{out}} = 3.64\,\mathrm{kW}, \eta = 0.95$				Optimum $\mathbf{p}^*_{\mathrm{B2}}$ $\bar{p}_{\mathrm{out}} = 5.08\,\mathrm{kW}, \eta = 0.94$				Optimum $\mathbf{p}^*_{\mathrm{B3}}$ $\bar{p}_{\mathrm{out}} = 5.43\,\mathrm{kW}, \eta = 0.93$				Optimum $\mathbf{p}^*_{\mathrm{B4}}$ $\bar{p}_{\mathrm{out}} = 6.46\,\mathrm{kW}, \eta = 0.92$			
m	1	2	3	4	1	2	3	4	1	2	3	4	1	2	3	4
N_m	15	15	15	5	15	15	15	5	15	15	14	4	13	13	10	4
r_m [cm]	25	24.9	24.9	20.1	25	24.9	25	18.3	25	24.9	25	19.4	25	25	25	19.5
z_m [cm]	0	4.08	34.2	39	0	3.83	33.9	38.8	0	3.9	34	38.8	0	3.69	33.7	38.7
f_m [kHz]	114	100	92	112	118	102	91.7	109	113	103	91.9	110	104	109	91.3	108
L_{mm} [μH]	157	156	157	20.8	157	156	157	18.3	157	156	142	13.6	128	128	86.3	13.7
C_m [nF]	12.4	16.2	19.1	96.7	11.6	15.7	19.2	115	12.6	15.2	21.1	153	18.4	16.6	35.2	160
R_m [mΩ]	118	118	118	105	118	118	118	105	118	118	117	104	116	116	113	104
k_{1m} [%]	-	61.2	6.9	4.1	-	62.9	7.0	3.7	-	62.5	7.0	3.9	-	62.5	6.9	3.9
k_{2m} [%]	-	-	8.7	5.1	-	-	8.7	4.6	-	-	8.7	4.8	-	-	8.5	4.8
k_{3m} [%]	-	-	-	46.5	-	-	-	41.2	-	-	-	42.9	-	-	-	39.0

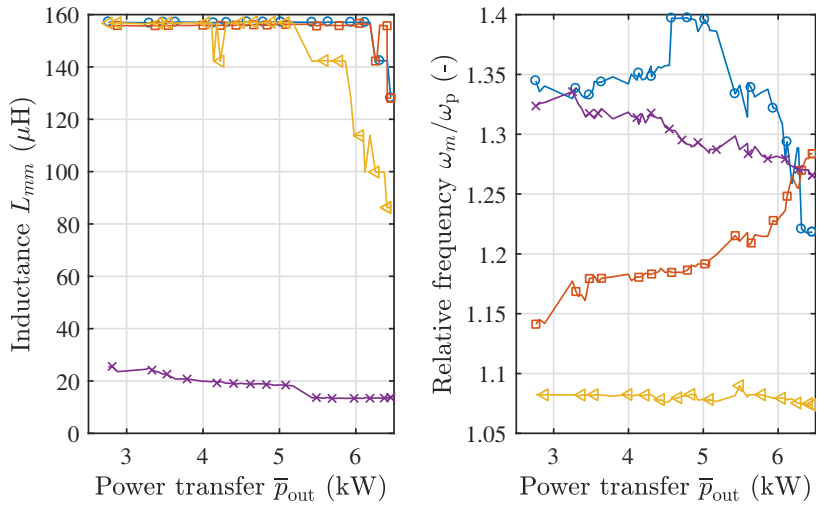

Figure 8. Optimized circuit parameters as the Pareto front in Figure 7 is traversed for $d/r_{\max} = 1.2$: (a) Inductance L_{mm}. (b) Resonance frequency $\omega_m/\omega_{\mathrm{p}}$ that also determines the capacitance $C_m = 1/(\omega_m^2 L_{mm})$. The glyphs correspond to the different resonators as indexed in Figure 2(b): ($\circ$) $m = 1$; ($\square$) $m = 2$; ($\triangleleft$) $m = 3$; and ($\times$) $m = 4$.

also find that the corresponding load impedance $Z_{\mathrm{B}} = R_{\mathrm{B}} + jX_{\mathrm{B}}$ at the terminals B_1-B_2 in Figure 2(b) is inductive for the battery load, where the resistive and reactive parts are comparable. Consequently, the approximate equivalent load resistance [8, 29] given by $R_{\mathrm{L}} = (\pi\mathcal{E}_{\mathrm{B}})^2/(8\,\bar{p}_{\mathrm{out}})$ must be generalized to an appropriately selected equivalent load impedance Z_{L}, should optimization of a WPT system with battery load based on a linear circuit model be accurate.

Next, we compute the equivalent load impedance Z_{A} for the fundamental frequency ω_{p}. Figure 9 shows Z_{A} as we traverse the Pareto front in Figure 7 for $d/r_{\max} = 1.2$ and $d/r_{\max} = 0.8$. Similarly as for the time-harmonic case, we note that Z_{A} is primarily resistive, although larger deviations from $X_{\mathrm{A}} = 0$ are present, which is particularly true for $d/r_{\max} = 1.2$. Although a clear decrease in efficiency is noted between the different transfer distances, we observe no significant difference in Z_{A} in the range $4\,\mathrm{kW} \leq \bar{p}_{\mathrm{out}} \leq 6\,\mathrm{kW}$ in Figure 9. Consequently, it appears important to effectively load the generator by a resistive load $Z_{\mathrm{A}} \simeq R_{\mathrm{A}} = \tilde{u}_{\mathrm{G}}^2/\bar{p}_{\mathrm{out}}$ to achieve optimal power transfer, but it is not a sufficient condition to assure that also the WPT system efficiency is optimal.

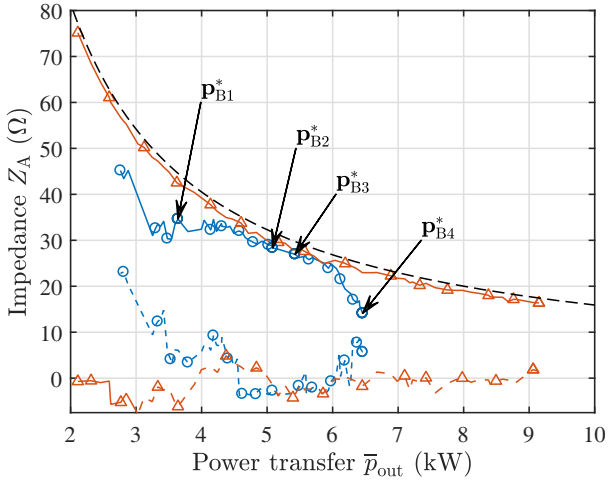

Figure 9. Impedance Z_A as a function of power delivered to the battery as the Pareto front in Figure 7 is traversed for: (○) $d/r_{max} = 1.2$; and (△) $d/r_{max} = 0.8$. The impedances are computed for the fundamental frequency as described in Section 3.1.1. The real part of the impedance is described by the solid curve and the imaginary part by the dashed curve. The black dash-dotted curve shows the load impedance $Z_A = R_A = \tilde{u}_G^2/\bar{p}_{out}$ for a simple generator and load model.

4.4. Compensation Using C_1 for Inductive Operation

During operation of the power inverter, we require that its load is inductive, which implies that the equivalent load impedance $Z_A = R_A + jX_A$ has a positive reactance X_A. If the equivalent load of the power inverter is capacitive with $X_A < 0$, a rather simple counter measure is to decrease the resonance frequency frequency $f_1 = 1/(2\pi\sqrt{L_{11}C_1})$ of the first resonant circuit by increasing the capacitance C_1. We stress that such a compensation typically does not decrease the system performance for the optima presented here, and if necessary, more elaborate compensation schemes that vary all four capacitors can be exploited [22].

As an example, we consider the optimized system $\mathbf{p}^*_{B4}$ during start-up, where the power inverter voltage U_0 is increased up to U_0^* as determined by the optimization problem in Eq. (12). The solid curves in Figure 10(a) presents Z_A as U_0 is increased from 50 V to 380 V. Here, the reactance X_A is negative for $U_0 < 320$ V and, thus, compensation is necessary for inductive operation of the power inverter. The dashed curves in Figure 10(a) show Z_A for a simple and ad-hoc compensation scheme, where C_1 is changed such that f_1 is increased linearly from $0.85f_1^*$ at $U_0 = 50$ V to f_1^* at $U_0 = 380$ V given the optimized frequency $f_1^* = 104$ kHz. It is clear that this simple measure yields $X_A > 0$ for all U_0.

Figure 10(b) shows the system performance by solid curves for the uncompensated case and by the dashed curves using the C_1 compensation scheme. In contrast with the uncompensated case, it is possible to achieve high efficiency also for the range $100\,\text{V} < U_0 < 170\,\text{V}$ using the compensation scheme. In practice, a control system could change C_1 to achieve sufficiently good performance and, if necessary, the capacitances of the other resonators could also be adjusted as demonstrated in [22].

4.5. Characteristic Charging Behavior for Optimized System

For a lithium-ion battery, a charge cycle typically contains two distinct parts. For the first part, the current is kept constant, and the voltage is increased from about $3\mathcal{E}_B^{max}/4$ (for a deeply discharged battery) to $\mathcal{E}_B^{max}$, where $\mathcal{E}_B^{max}$ is the electromotive force of the battery when it is fully charged. The first part is therefore referred to as constant-current charging, and it is used from low values of the state-of-charge (SOC) up to some intermediate level of SOC. For the second part, the voltage is kept constant at $\mathcal{E}_B^{max}$, and the current is decreased as the SOC of the battery increases up to 100%, which is referred to as constant-voltage charging. In practice, battery charging is considerably more complicated,

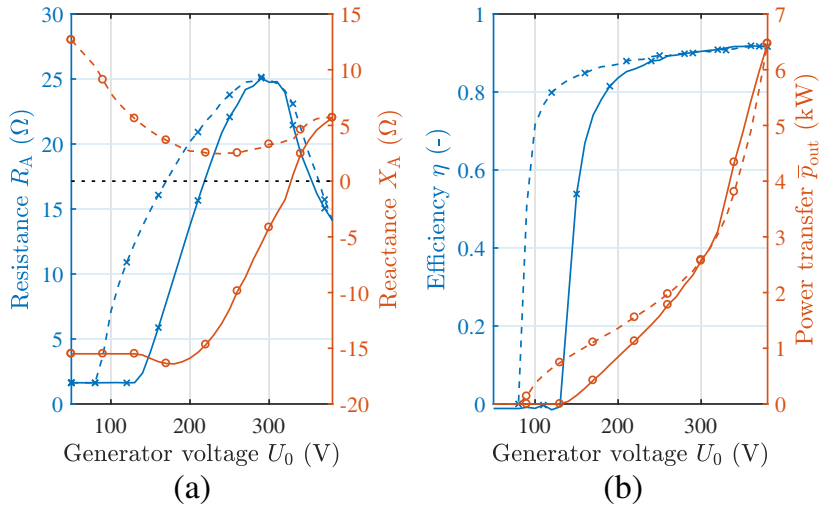

Figure 10. (a) Impedance Z_A in terms of resistance R_A (×) and reactance X_A (○) versus U_0. (b) Efficiency (×) and power transfer to the battery (○) versus U_0. Both figures show the results for the transfer distance $d/r_{max} = 1.2$ using the design parameters for optimum $\mathbf{p}^*_{B4}$ by solid curves. The dashed curves show the corresponding results using a simple compensation scheme for the optimum $\mathbf{p}^*_{B4}$ where C_1 is changed such that f_1 is linearly increased from $0.85f_1^*$ at $U_0 = 50\,\mathrm{V}$ to f_1^* at $U_0 = 380\,\mathrm{V}$. The horizontal dashed-dotted line in (**a**) shows $X_A = 0$.

and various active circuits are used to help achieve a safe and reliable charging according to a specific charging cycle.

As an example, we consider the optimized design $\mathbf{p}^*_{B4}$ and its performance characteristics in the context of constant-current and constant-voltage charging, where the design $\mathbf{p}^*_{B4}$ is optimized for $\mathcal{E}_B = \mathcal{E}_B^{max} = 380\,\mathrm{V}$. Figure 11 shows the system efficiency and power delivered to the battery as a function of the voltage amplitude $U_0 \leq U_0^*$, where results for $\mathcal{E}_B = 320\,\mathrm{V}$, $350\,\mathrm{V}$ and $380\,\mathrm{V}$ are shown. We note that the efficiency and power transfer characteristics are rather similar for the different electromotive forces of the battery, where these deal with a range $0.85\mathcal{E}_B^{max} < \mathcal{E}_B \leq \mathcal{E}_B^{max}$. Consequently, the optimized system $\mathbf{p}^*_{B4}$ can follow an increasing $\mathcal{E}_B$ given an increasing amplitude $U_0 = U_0^*$ for the

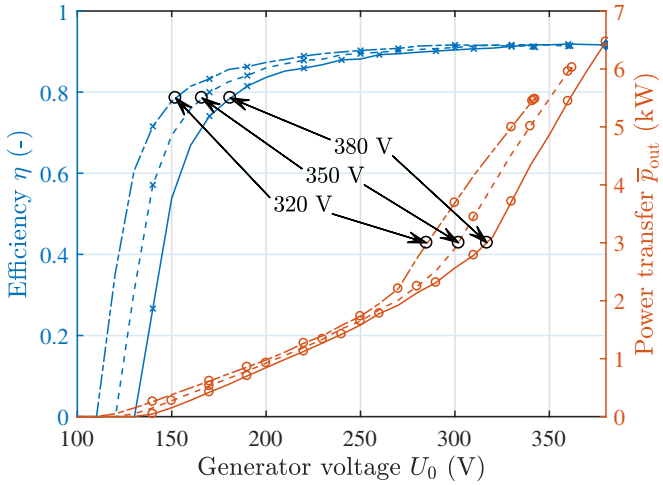

Figure 11. System efficiency (×) and power transfer to the battery (○) as a function of the generator voltage U_0 for the transfer distance $d/r_{max} = 1.2$ using the design parameters for optimum $\mathbf{p}^*_{B4}$ at three different battery voltage levels: solid $380\,\mathrm{V}$; dashed $350\,\mathrm{V}$; and dash-dotted $320\,\mathrm{V}$.

power inverter, and this solution may work rather well for constant-current charging of a lithium-ion battery pack, should the WPT system be equipped with a suitable control system and active circuitry. Next, we note that the constant-voltage charging is described approximately by the case $\mathcal{E}_{\mathrm{B}} = \mathcal{E}_{\mathrm{B}}^{\max}$ in Figure 11, where the output voltage of the smoothing filter is rather constant, and the current through the rectifier (and into the battery) is approximately proportional to $\bar{p}_{\mathrm{out}}$. Again, a suitable control system and active circuitry would be necessary. In practice, the power inverter's duty cycle could be changed instead of the peak voltage U_0.

5. CONCLUSIONS

We have presented an optimization framework that yields competitive designs for a WPT system that features real-world challenges: 1) a nonlinear load with rectifier, smoothing filter and battery; 2) optimization with respect to multiple objectives that contrast system efficiency and power delivered to the battery; 3) realistic design-constraints that express component limitations, restrictions on size and current overtones in the coils; and 4) a fully populated inductance matrix that gives a complete port-to-port representation based on the magnetic field problem for the full set of coils of the WPT system. We find our optimization approach attractive in the sense that it exposes the important performance trade-offs necessary to consider in many WPT applications. In particular, we note that the current and voltage constraints limit the maximum realizable power transfer in a complicated manner.

For a family of test problems motivated by wireless charging systems for vehicles, we present Pareto fronts that contrast the system efficiency versus the power delivered to the battery for a WPT system with four magnetically coupled resonators. The Pareto fronts are computed for a range of distances $0.8 \leq d/r_{\max} \leq 1.6$, where $r_{\max} = 25\,\mathrm{cm}$ is the maximum radius of the coils, and d is the power transfer distance.

For the separate resonators indexed by m, we note that our optimized results feature resonance frequencies $\omega_m = 1/\sqrt{L_{mm}C_m}$ that vary as the Pareto front is traversed and, in addition, that these resonance frequencies tend to take values that do not coincide with the excitation frequency ω_{p} of the generator. In contrast, many analytical results found in the literature assume that $\omega_m = \omega_{\mathrm{p}}$ for all m, and thus, we conclude that such choices indeed yield relatively simple analytical expressions that are easy to work with but may very well also be sub-optimal for a constrained WPT system.

The maximum realizable power transfer is found to primarily depend on the voltage and current constraints for the circuit for a given value of $d/r_{\max}$, and we find that the four magnetically coupled resonators and load behave approximately as an equivalent resistance connected to the power inverter after optimization. However, we find that the corresponding construction for the rectifier, smoothing filter and battery requires an equivalent impedance, where the inductive reactance is comparable to the resistance. Furthermore, we consider a battery load with its electromotive force $\mathcal{E}_{\mathrm{B}}$ in the range $310\,\mathrm{V} \leq \mathcal{E}_{\mathrm{B}} \leq 390\,\mathrm{V}$ and conclude that an optimized WPT system can achieve similar performance for this entire range, should it be optimized for the largest value of $\mathcal{E}_{\mathrm{B}}$. Thus, the optimized WPT systems could be used to supply power to a battery load with varying state-of-charge by controlling the voltage of the power inverter.

ACKNOWLEDGMENT

This work was funded by the Swedish Energy Agency in the project "Säker induktiv energiöverföring för elfordon – Safe Wireless Energy (SAWE)", which has the project number 38577-1. The computations were performed on resources at Chalmers Center for Computational Science and Engineering (C3SE) provided by the Swedish National Infrastructure for Computing (SNIC).

APPENDIX A. CONSTRAINED GENERATOR WITH RESISTIVE LOAD

To analyze the effects of voltage and current constraints on the generator, we consider the simple model where the generator is modelled as a voltage source $\tilde{u}_{\mathrm{G}}$ in series with an internal resistance R_{G}, and a load resistance R_{A} is connected to its terminals. For a well-functioning WPT system with low current overtones, this is a rather useful model despite its simplicity, since the optimized impedance

on the output of the power-inverter's terminals is approximately real. We let the effective value of the generator voltage and current be constrained by

$$\tilde{u}_{\mathrm{G}} \leq \tilde{u}_{\mathrm{G}}^{\max} \qquad \text{and} \qquad \tilde{\imath}_{\mathrm{G}} \leq \tilde{\imath}_{\mathrm{G}}^{\max} \tag{A1}$$

where $\tilde{u}_{\mathrm{G}}^{\max}$ and $\tilde{\imath}_{\mathrm{G}}^{\max}$ are constants derived from the physical components that are used in the power inverter. According to Ohm's law $\tilde{u}_{\mathrm{G}} = R_{\mathrm{tot}}\tilde{\imath}_{\mathrm{G}}$, the generator voltage is bounded by $\tilde{u}_{\mathrm{G}} \leq \tilde{u}_{\mathrm{G}}^{\max} = \min(\tilde{u}_{\mathrm{G}}^{\max}, R_{\mathrm{tot}}\tilde{\imath}_{\mathrm{G}}^{\max})$, where $R_{\mathrm{tot}} = R_{\mathrm{G}} + R_{\mathrm{A}}$. Thus, the generator's input power $\bar{p}_{\mathrm{in}}^{\max}$ and the output power $\bar{p}_{\mathrm{out}}^{\max}$ delivered to the load are bounded by

$$\bar{p}_{\mathrm{in}} \leq \bar{p}_{\mathrm{in}}^{\max} = \min\left((\tilde{u}_{\mathrm{G}}^{\max})^2/R_{\mathrm{tot}},\, R_{\mathrm{tot}}(\tilde{\imath}_{\mathrm{G}}^{\max})^2\right), \tag{A2}$$

$$\bar{p}_{\mathrm{out}} \leq \bar{p}_{\mathrm{out}}^{\max} = \min\left((\tilde{u}_{\mathrm{G}}^{\max})^2 R_{\mathrm{A}}/R_{\mathrm{tot}}^2,\, R_{\mathrm{A}}(\tilde{\imath}_{\mathrm{G}}^{\max})^2\right), \tag{A3}$$

which yields the efficiency $\eta = \bar{p}_{\mathrm{out}}/\bar{p}_{\mathrm{in}} = R_{\mathrm{A}}/R_{\mathrm{tot}}$.

According to Eq. (A1), the maximum possible generator power is $\bar{p}_{\mathrm{G}}^{\max} = \tilde{u}_{\mathrm{G}}^{\max}\tilde{\imath}_{\mathrm{G}}^{\max}$, for which we define the efficiencies

$$\chi_{\mathrm{G}} = \frac{\bar{p}_{\mathrm{in}}^{\max}}{\bar{p}_{\mathrm{G}}^{\max}} = \min\left(\xi/R_{\mathrm{tot}},\, R_{\mathrm{tot}}/\xi\right), \tag{A4}$$

$$\chi_{\mathrm{A}} = \frac{\bar{p}_{\mathrm{out}}^{\max}}{\bar{p}_{\mathrm{G}}^{\max}} = \min\left(R_{\mathrm{A}}\xi/R_{\mathrm{tot}}^2,\, R_{\mathrm{A}}/\xi\right), \tag{A5}$$

where $\xi = \tilde{u}_{\mathrm{G}}^{\max}/\tilde{\imath}_{\mathrm{G}}^{\max}$. For $\xi = R_{\mathrm{tot}}$, we find that both the constraints in Eq. (A1) are active simultaneously which yields $\chi_{\mathrm{G}} = 1$ and $\chi_{\mathrm{A}} = R_{\mathrm{A}}/R_{\mathrm{tot}} = \eta$. For $\xi \neq R_{\mathrm{tot}}$, only one of the two constraints in Eq. (A1) is active, and the generator cannot be fully utilized.

Next, we search for the maximum power transfer to R_{A} by maximizing $\chi_{\mathrm{A}} = \min(\chi_{\mathrm{A},1}, \chi_{\mathrm{A},2})$ with respect to R_{A}. We find two cases: 1) if $\xi \leq 2R_{\mathrm{G}}$, then $\chi_{\mathrm{A}}^{\max} = \xi/(4R_{\mathrm{G}})$ at $R_{\mathrm{A}} = R_{\mathrm{G}}$ from the maximum of $\chi_{\mathrm{A},1}$; and 2) if $\xi \geq 2R_{\mathrm{G}}$, then $\chi_{\mathrm{A}}^{\max} = 1 - R_{\mathrm{G}}/\xi$ at $R_{\mathrm{A}} = \xi - R_{\mathrm{G}}$ from the intersection between $\chi_{\mathrm{A},1}$ and $\chi_{\mathrm{A},2}$. Our analysis leads to the rather interesting conclusion that the maximum power transfer occurs at the effective load resistance $R_{\mathrm{A}}^{*} = \tilde{u}_{\mathrm{G}}^{\max}/\tilde{\imath}_{\mathrm{G}}^{\max} - R_{\mathrm{G}}$ for $\tilde{u}_{\mathrm{G}}^{\max}/\tilde{\imath}_{\mathrm{G}}^{\max} \geq 2R_{\mathrm{G}}$. We emphasize that R_{A}^{*} does not coincide with the conventional impedance matching condition $R_{\mathrm{A}}^{*} = R_{\mathrm{G}}$, which only applies to $\tilde{u}_{\mathrm{G}}^{\max}/\tilde{\imath}_{\mathrm{G}}^{\max} \leq 2R_{\mathrm{G}}$.

REFERENCES

1. Jawad, A. M., R. Nordin, S. K. Gharghan, H. M. Jawad, and M. Ismail, "Opportunities and challenges for near-field wireless power transfer: A review," *Energies*, Vol. 10, No. 7, 2017.
2. Kazmierkowski, M. P. and A. J. Moradewicz, "Unplugged but connected: Review of contactless energy transfer systems," *IEEE Ind. Electron. Mag.*, Vol. 6, 47–55, Dec. 2012.
3. Kim, S., H.-H. Park, J. Kim, J. Kim, and S. Ahn, "Design and analysis of a resonant reactive shield for a wireless power electric vehicle," *IEEE Trans. Microw. Theory Tech.*, Vol. 62, 1057–1066, Apr. 2014.
4. Musavi, F. and W. Eberle, "Overview of wireless power transfer technologies for electric vehicle battery charging," *IET Power Electronics*, Vol. 7, 60–66, Jan. 2014.
5. Kurs, A., A. Karalis, R. Mofatt, J. D. Joannopoulos, P. Fisher, and M. Soljacic, "Wireless power transfer via strongly coupled magnetic resonances," *Science*, Vol. 317, 83–86, Jul. 2007.
6. Kesler, M., "Highly resonant wireless power transfer: Safe, efficient, and over distance," *Tech. Rep.*, WiTricity Corporation, Watertown, MA, USA, 2013.
7. Sallan, J., J. L. V. A. Llombart, and J. F. Sanz, "Optimal design of ICPT systems applied to electric vehicle battery charge," *IEEE Trans. Ind. Electron.*, Vol. 56, 2140–2149, Jun. 2009.
8. Bosshard, R., J. W. Kolar, J. Mühlethaler, I. Stevanović, B. Wunsch, and F. Canales, "Modeling and η-α-Pareto optimization of inductive power transfer coils for electric vehicles," *IEEE J. Emerg. Sel. Topics Power Electron.*, Vol. 3, No. 1, 50–64, 2015.
9. Kiani, M. and M. Ghovanloo, "The circuit theory behind coupled-mode magnetic resonance-based wireless power transmission," *IEEE Trans. Circuits Syst. I*, Vol. 59, 2065–2074, Sep. 2012.

10. Bou, E., E. Alarcon, and J. Gutierrez, "A comparison of analytical models for resonant inductive coupling wireless power transfer," *PIER Symposium Proceedings*, 689–693, Aug. 2012.
11. Hui, S. Y. R., W. Zhong, and C. K. Lee, "A critical review of recent progress in mid-range wireless power transfer," *IEEE Trans. Power Electron.*, Vol. 29, No. 9, 4500–4511, 2014.
12. Zhong, W., C. K. Lee, and S. Y. R. Hui, "General analysis on the use of Tesla's resonators in domino forms for wireless power transfer," *IEEE Trans. Ind. Electron.*, Vol. 60, 261–270, Jan. 2013.
13. Alberto, J., U. Reggiani, L. Sandrolini, and H. Albuquerque, "Fast calculation and analysis of the equivalent impedance of a wireless power transfer system using an array of magnetically coupled resonators," *Progress In Electromagnetics Research B*, Vol. 80, 101–112, 2018.
14. Chu, J., W. Gu, W. Niu, and A. Shen, "Frequency splitting patterns in wireless power relay transfer," *IET Circuits, Devices & Systems*, Vol. 8, No. 6, 561–567, 2014.
15. Bosshard, R. and J. W. Kolar, "Multi-objective optimization of 50 kW/85 kHz IPT system for public transport," *IEEE J. Emerg. Sel. Top. Power Electron.*, Vol. 4, 1370–1382, Dec. 2016.
16. Haupt, R. L., "An introduction to genetic algorithms for electromagnetics," *IEEE AP Magazine*, Vol. 37, No. 2, 7–15, 1995.
17. Rahmat-Samii, Y. and E. Michielssen, eds., *Electromagnetic Optimization by Genetic Algorithms*, 1st Edition, John Wiley & Sons, Inc., New York, NY, USA, 1999.
18. Cheon, S., Y.-H. Kim, S.-Y. Kang, M. L. Lee, J.-M. Lee, and T. Zyung, "Circuit-model-based analysis of a wireless energy-transfer system via coupled magnetic resonances," *IEEE Trans. Ind. Electron.*, Vol. 58, 2906–2914, Jul. 2011.
19. Sample, A. P., D. A. Meyer, and J. R. Smith, "Analysis, experimental results, and range adaptation of magnetically coupled resonators for wireless power transfer," *IEEE Trans. Ind. Electron.*, Vol. 58, No. 2, 544–554, 2011.
20. SAE Standard, "J2954, wireless power transfer for light-duty plug-in/electric vehicles and alignment methodology," 2016.
21. Jackson, J. D., *Classical Electrodynamics*, 3rd Edition, Willey, New York, 1999.
22. Winges, J., T. Rylander, C. Petersson, C. Ekman, L.-Å. Johansson, and T. McKelvey, "System identification and tuning of wireless power transfer systems with multiple magnetically coupled resonators," *Trans. Environ. Electr. Eng.*, Vol. 2, No. 2, 86–92, 2018.
23. Hamnerius, Y., T. Nilsson, T. Rylander, J. Winges, C. Ekman, C. Petersson, and T. Fransson, "Design of safe wireless power transfer systems for electric vehicles," *Proc. 2nd URSI AT- RASC*, Grand Canaria, Spain, May 2018.
24. Bosshard, R. and J. W. Kolar, "All-SiC 9.5 kW/dm 3 on-board power electronics for 50 kW/85 kHz automotive IPT system," *IEEE J. Emerg. Sel. Top. Power Electron.*, Vol. 5, 419–431, Mar. 2017.
25. Tamaki, H., H. Kita, and S. Kobayashi, "Multi-objective optimization by genetic algorithms: A review," *Proc. IEEE Int. Conf. Evolutionary Computation*, 517–522, May 1996.
26. Press, W. H., S. A. Teukolsky, W. T. Vetterling, and B. P. Flannery, *Numerical Recipes in C: The Art of Scientific Computing*, 2nd Edition, Cambridge University Press, New York, NY, 1992.
27. Abramowitz, M. and I. A. Stegun, *Handbook of Mathematical Functions: With Formulas, Graphs, and Mathematical Tables*, National Bureau of Standards, 1965.
28. Brocard, G., *The LTSpice IV Simulator: Manual, Methods and Applications*, Swiridoff Verlag, Künzelsau, Germany, 2013.
29. Steigerwald, R., "A comparison of half-bridge resonant converter topologies," *IEEE Trans. Power Electron.*, Vol. 3, 174–182, Apr. 1988.